The Planetary Science Journal, 1:18 (15pp), 2020 June https://doi.org/10.3847/PSJ/ab91aa

Embryo Formation with GPU Acceleration: Reevaluating the Initial Conditions for Terrestrial Accretion

Matthew S. Clement[1,2], Nathan A. Kaib[2], and John E. Chambers[1]
[1] Department of Terrestrial Magnetism, Carnegie Institution for Science, 5241 Broad Branch Road, NW, Washington, DC 20015, USA;
mclement@carnegiescience.edu
[2] HL Dodge Department of Physics Astronomy, University of Oklahoma, Norman, OK 73019, USA

Received 2020 January 21; revised 2020 May 6; accepted 2020 May 7; published 2020 June 2

Abstract

The solar system's terrestrial planets are thought to have accreted over millions of years out of a sea of smaller embryos and planetesimals. Because it is impossible to know the surface density profile for solids and size frequency distribution in the primordial solar nebula, distinguishing between the various proposed evolutionary schemes has historically been difficult. Nearly all previous simulations of terrestrial planet formation assume that Moon- to Mars-massed embryos formed throughout the inner solar system during the primordial gas-disk phase. However, validating this assumption through models of embryo accretion is computationally challenging because of the large number of bodies required. Here, we reevaluate this problem with GPU-accelerated, direct N-body simulations of embryo growth starting from $r \sim 100$ km planetesimals. We find that embryos emerging from the primordial gas phase at a given radial distance already have masses similar to the largest objects at the same semimajor axis in the modern solar system. Thus, Earth and Venus attain ~50% of their modern mass, Mars-massed embryos form in the Mars region, and Ceres-massed objects are prevalent throughout asteroid belt. Consistent with other recent work, our new initial conditions for terrestrial accretion models produce markedly improved solar system analogs when evolved through the giant impact phase of planet formation. However, we still conclude that an additional dynamical mechanism such as giant planet migration is required to prevent Earth-massed Mars analogs from growing.

Unified Astronomy Thesaurus concepts: Inner planets (797); Solar system planets (1260); Planetary system formation (1257); Solar system formation (1530); Planetary science (1255); Planetesimals (1259); Protoplanetary disks (1300)

1. Introduction

Since advances in computing power led to the widespread availability of open-source symplectic integrators (Wisdom & Holman 1991; Duncan et al. 1998; Chambers 1999), numerous theoretical studies have been dedicated to understanding the origins of the solar system's terrestrial architecture (for recent reviews on the topic, see Izidoro & Raymond 2018; Raymond et al. 2018). Broadly speaking, a successful model for the inner solar system must reconcile the differences in mass distribution and orbital excitation between the modern system and the presumed primordial solar nebula (e.g., Weidenschilling 1977a). Of particular interest in the literature are the order-of-magnitude differences between the masses of Mercury and Mars and the neighboring Earth and Venus (Chambers 2001; Raymond et al. 2009; Lykawka & Ito 2019), the disparity of four orders of magnitude mass between the asteroid belt and planetary regimes (O'Brien et al. 2007; Izidoro et al. 2015; Clement et al. 2019c), and the plethora of high orbital eccentricities and inclinations in the asteroid belt (Petit et al. 2001; Morbidelli et al. 2010; Deienno et al. 2016). While there are many compelling models and solutions to these issues, nonuniform disk conditions (Hansen 2009; Izidoro et al. 2014), the influence of the giant planets (Walsh 2009; Raymond et al. 2009; Lykawka & Ito 2013; Bromley & Kenyon 2017), and different modes of accretion (Levison et al. 2015; Morbidelli et al. 2015; Drażkowska et al. 2016) feature prominently in most proposed evolutionary scenarios. However, many models are based on an assumption that Moon- to Mars-massed planet-forming embryos were abundant throughout the terrestrial disk (Kokubo & Ida 2002), which is in conflict with modern high-resolution simulations of embryo formation (Carter et al. 2015; Walsh & Levison 2019). This is partially a consequence of the fact that owing to limits in computing power, the various phases of planet growth (planetesimal formation, embryo formation, and the giant impact phase) are often treated separately. We briefly summarize each phase of accretion below (not discussed here, but still relevant for the solar system are gas accretion and planet migration; see reviews in Morbidelli et al. 2012; Raymond et al. 2018):

1.1. Planetesimal Formation

Large infrared excesses in observed protoplanetary nebulae (Briceño et al. 2001) imply that the majority of the solid mass in young planet-forming disks is concentrated in submicron-sized dust grains. Population studies of gaseous disk ages (Haisch et al. 2001) indicate that they do not persist for longer than a few million years. Because ages of iron meteorites indicate that their primitive parent bodies accreted rapidly ($\lesssim$5 Myr, apparently predating the appearance of chondrules: Kleine et al. 2005), the transition from dust to 10–100 kilometer-scale planetesimals must have occurred rapidly, while gas was still present in the system. Additionally, surveys of protostellar disks indicate that they possess significantly higher dust masses than protoplanetary disks (Tobin et al. 2020). This result seems to imply that the conversion of dust to larger solid bodies occurs rapidly, and in conjunction with the earliest epochs of star formation.

Dust grains can grow via various processes including coagulation (Xiang et al. 2019), aggregation, and compaction (Wetherill 1980a; Dominik et al. 2007). However, explaining growth beyond meter scales (the so-called meter-barrier: Weidenschilling 1977b; Birnstiel et al. 2012) is difficult because millimeter-sized bodies experience significant aerodynamic drag, causing them to orbit at sub-Keplerian velocities and migrate inward (Whipple 1972). One intriguing solution to this issue might be direct formation via gravitational collapse. If dust particles are sufficiently concentrated relative to the gas, they can clump together and form $D \sim 100$ km planetesimals rapidly via gravitational instability (Johansen et al. 2015). While the “streaming instability” scenario offers a compelling resolution to the meter-barrier problem, the specific properties (radial location, final masses, and formation time) of the resulting primordial generation of planetesimals are dependent on unconstrained disk parameters (Drażkowska et al. 2016; Carrera et al. 2017; Abod et al. 2019).

1.2. Embryo Formation

Planetesimals continue to grow larger throughout the gas-disk phase by direct accretion of other planetesimals (Wetherill & Stewart 1993; Kokubo & Ida 1998) and inward-drifting "pebbles" of approximately meter-scale sizes (the radial flux of which is still debated: Johansen & Lacerda 2010; Chambers 2016; Ida & Guillot 2016). This growth phase is highly efficient as long as the relative velocities in the region are low. The largest local planetesimal gravitationally focuses (Chambers 2006) the incoming flux of planetesimals and pebbles, causing runaway growth to ensue (Kokubo & Ida 1996). Eventually, the oligarch planetesimals grow large enough to excite the orbits of nearby planetesimals and inhibit accretion (Kokubo & Ida 2000). Growth can continue beyond this stage if the pebble flux is great enough (Lambrechts & Johansen 2014) because pebbles are sufficiently small for gas-disk interactions to damp their orbits. Eventually, pebble accretion shuts off when an embryo grows large enough (“pebble isolation mass:” Morbidelli & Nesvorny 2012) to induce a pressure gradient in the disk that prohibits inward pebble drift. Recent high-resolution simulations in Wallace & Quinn (2019) uncovered an additional growth mode that occurs in the vicinity of massive oligarchs as small planetesimals are stacked inside of nearby first-order mean motion resonances (MMR); thereby accelerating their growth toward intermediate masses and inducing a corresponding bump in the planetesimal size frequency distribution (SFD).

1.3. Giant Impact Phase

In the final phase of terrestrial growth, the embryo and planetesimal populations emerging from the gas disk collisionally assemble over ∼100 Myr timescales (Wetherill 1978; Chambers 2001; Raymond et al. 2009). By and large, numerical models of the “giant impact” phase report timescales for the epoch’s completion consistent with the geologically inferred timing of the Moon-forming impact (∼50–150 Myr; Kleine et al. 2009). Moreover, it is within this ultimate stage of accretion that many authors have proposed solutions to the aforementioned mass and orbital excitation disparities in the inner solar system. Accounting for hit-and-run collisions (Chambers 2013; Clement et al. 2019b) and dynamical friction induced by small bodies (O’Brien et al. 2006; Raymond et al. 2006) can result in analog terrestrial planets with more realistic dynamically cold orbits. Furthermore, the giant planet instability (the “Nice Model” of Tsiganis et al. 2005; Levison et al. 2008; Nesvorný & Morbidelli 2012) is typically invoked to explain the asteroid belt’s excited state (Roig & Nesvorný 2015; Deienno et al. 2016; Deienno et al. 2018) and (at least some of) its primordial depletion (Morbidelli et al. 2010; Clement et al. 2019c). Reconciling the Earth-Mars mass disparity, however, has led to the development of a multitude of different models. It should also be mentioned here that collisional fragmentation (Chambers 2013) plays a role in the giant impact phase of terrestrial growth, the degree to which is a topic of continued debate (for recent works espousing differing viewpoints, we refer to Clement et al. 2019b; Deienno et al. 2019; Kobayashi et al. 2019). Specifically, a large, fragmenting collision (Asphaug & Reufer 2014) is a potentially viable explanation for Mercury’s large iron-rich core (Jackson et al. 2018).

1.4. Small-Mars Problem

Solutions to the small-Mars problem (Wetherill 1991) generally fall in to one of two categories. In the first class of models (e.g., Hansen 2009; Raymond & Izidoro 2017), the outer terrestrial disk is already depleted during the primordial gas-disk phase, and the terrestrial planets form out of a narrow annulus of material. In one such scenario (the so-called “Grand Tack” model of Walsh et al. 2011; Jacobson & Morbidelli 2014; Walsh & Levison 2016), the inner disk is truncated when Jupiter migrates into and subsequently back out of the terrestrial region. Thus, Mars forms rapidly as a “stranded embryo” (Dauphas & Pourmand 2011; Izidoro et al. 2014). In contrast, the second class of models invokes a dynamical mechanism to starve the region of material during the planet formation process (Raymond et al. 2009). Typically, the influence of Jupiter and Saturn perturbs objects in the region, and inhibits Mars’ formation. Resonance sweeping or crossing (Lykawka & Ito 2013; Bromley & Kenyon 2017), primordially excited giant planet orbits (Raymond et al. 2009; Lykawka & Ito 2019), and the Nice Model instability (Clement et al. 2018) have all been shown to substantially restrict Mars’ growth. In particular, the “Early Instability” scenario argues that a Nice Model timed ∼1–5 Myr (Clement et al. 2019b) after gas-disk dispersal explains Mars’ rapid inferred geologic formation time (Dauphas & Pourmand 2011; Kruijer et al. 2017). However, each model should be considered in the appropriate context given the fact that Mercury’s low mass and orbit are still very low probability outcomes of numerical simulations (Sarid et al. 2014; Clement et al. 2019a).

1.5. This Work

With few exceptions, the aforementioned N-body studies of the giant impact phase all place large embryos throughout the terrestrial disk and modern asteroid belt. However, such initial conditions are at odds with semianalytic predictions of oligarchic growth (Kokubo & Ida 1998, 2000), as well as recent high-resolution studies of embryo formation within gaseous disks (Carter et al. 2015; Wallace & Quinn 2019;

Walsh & Levison 2019). In particular, it appears unlikely that the primordial asteroid belt region attained such an advanced evolutionary state during the gas-disk phase. In this paper we follow the complete growth of the terrestrial system starting from $r \sim 100$ km planetesimals accreting in a decaying gas disk (Morishima et al. 2010). It should be noted that as a tangentially related alternative to our proposed scenario, self-consistent pebble accretion (not considered in our work) simulations (e.g., Morbidelli et al. 2015) form embryos directly throughout the terrestrial disk.

Our current study is perhaps most similar to the recent work of Carter et al. (2015) and Walsh & Levison (2019), and we compare our results with both authors' findings throughout this manuscript. While Carter et al. (2015) used a parallelized *N*-body code (*PKDGRAV*: Richardson et al. 2000; Stadel 2001) with inflated planet radii and Walsh & Levison (2019) employed a Lagrangian integrator and tracer particles (the *LIPAD* code: Levison et al. 2012), we opt for a direct, GPU-accelerated *N*-body scheme (GENGA: Grimm & Stadel 2014) that fully resolves close encounters. Notably, we investigate the effects of Jupiter's and Saturn's presence, and use self-interacting planetesimals for much of the runaway growth phase. While we leave the full-resolution evolution of our generated distributions of embryos and planetesimals through the giant impact phase to a future paper, we perform an additional suite of simplified simulations of the final stage of accretion for a first-order approximation of the final system architectures.

2. Methods

To achieve sufficiently high particle resolution throughout the terrestrial disk, we begin by numerically integrating different radial annuli separately. As oligarchic growth ensues in each annulus, we begin to merge our simulations; combining and interpolating between individual annuli until the entire terrestrial disk is assembled in a single simulation at the $t = 1$ Myr. For each of the simulations that include gas drag, we use the GPU-parallelized hybrid symplectic integrator GENGA (Grimm & Stadel 2014). GENGA is based on the *Mercury* code of Chambers (1999), runs on all *Nvidia* GPUs, and is available to the public in an open-source format. In all of our simulations we employ a time step equal to ~5% that of the shortest orbital period, remove objects that pass within 0.1 au of the Sun (common practice in *N*-body studies of planet formation, see Chambers 2001), and consider particles ejected from the system at 100 au. We also incorporate a simple analytic gas-disk model (Morishima et al. 2010) that mimics the effects of aerodynamic drag (Adachi et al. 1976), e/i damping induced by tidal interactions between the gas disk and protoplanets (Tanaka et al. 2002), and the global nebular gravitational (Nagasawa et al. 2000) force by applying an additional acceleration to each body after the Keplerian drift kicks. In this model, gas dissipates exponentially in time and uniformly in space as

$$\Sigma_{\rm gas}(r,\,t) = \Sigma_{\rm gas}(1\ {\rm au},\,0)\left(\frac{r}{1\ {\rm au}}\right)^{-\alpha}\exp\left(-\frac{t}{\tau_{\rm gas}}\right) \quad (1)$$

.

While previous authors (Morishima et al. 2010; Walsh & Levison 2019) have investigated different gas densities and decay times, we limit our study to the nominal minimum mass solar nebula (MMSN; Hayashi 1981) because we are constricted by the availability of GPUs. Thus, for all of our integrations, we use a decay time of $\tau_{\rm gas} = 3$ Myr, an initial surface density of $\Sigma_{\rm gas}(1\ {\rm au},\,0) = 2000\ {\rm g\ cm^{-2}}$, and set $\alpha = 1$ (based on the nominal α of Morishima et al. 2010) .

Table 1
Summary of Annulus Edges and Centers for Simulations of Oligarchic Growth from 0 to 100 Kyr

Annulus	$a_{\rm in}$ (au)	$a_{\rm center}$ (au)	$a_{\rm out}$ (au)	N_f/N_i
1	0.48	0.50	0.52	0.06
2	0.9745	1.0	1.0255	0.27
3	1.4685	1.5	1.5315	0.51
4	1.9635	2.0	2.0365	0.68
5	2.9505	3.0	3.0495	0.88

Note. Each annulus contains 5000 fully self-gravitating objects and has a total mass of 0.1 $M_\oplus$. Note that the different annulus widths are a result of the $\Sigma \propto r^{-3/2}$ surface density profile.

2.1. Runaway Growth in the Inner Disk: 0–100 Kyr

We begin by following the evolution of five $0.1M_\oplus$ annuli located at 0.5, 1.0, 1.5, 2.0, and 3.0 au (see Table 1) for 100 Kyr. Each annulus is composed of 5000 fully self-gravitating equal-massed planetesimals on nearly circular coplanar orbits (we draw initial eccentricities and inclinations from Rayleigh distributions with $\sigma_e = 0.002$ and $\sigma_i = 0.2°$ as described in Ida 1990; Kokubo & Ida 1998). Thus, when we assume a nominal planetesimal density of 3.0 g cm^{-3}, each object has $D \approx 200$ km. Our annuli are derived from a terrestrial disk (0.5–4.0 au) that contains 5 $M_\oplus$ of solid material with a surface density profile that falls off radially as $r^{-3/2}$ (consistent with studies of terrestrial planet formation; Wetherill 1996; Chambers 2001; Raymond et al. 2009; Walsh & Levison 2019). To account for edge effects, we employ a boundary condition similar to that in Kokubo & Ida (2000). If a particle's semimajor axis passes beyond 0.005 au of either annulus edge, it is removed from the simulation and a new object is added at the opposite edge with inclination and eccentricity drawn from the annulus' in situ distributions. The largest error introduced by this choice of boundary condition is an artificial damping of orbits near the boundary edge because the objects with higher eccentricities are being removed. However, the gas-driven migration timescale for $r = 100$ km planetesimals (e.g., Weidenschilling 1977b) is greater than the nebular lifetime for our gas-disk model (Morishima et al. 2010). Moreover, radial scattering due to close encounters is significantly subdued in this phase of our simulations because eccentricities are highly damped. Therefore, in practice, this exchange of particles rarely occurs because orbits are highly damped.

2.2. Runaway Growth in the Outer Disk: 100–1000 Kyr

Because runaway growth ensues rapidly (Kokubo & Ida 1998) at small radial distances, the total number of particles in our $r = 0.5$, 1.0 and 1.5 au annuli is small enough at $t = 100$ Kyr ($N_f/N_i = 0.06$, 0.27, and 0.51, respectively) to begin interpolating between annuli. We generate seven wider annuli (Table 2 and Figure 1) based on the mass and orbital distributions within our inner three annuli after 100 Kyr of evolution. Combined, these new simulations span the entire radial range of 0.48–1.65 au. To accomplish this interpolation,

Table 2
Summary of Annulus Edges and Total Particle Numbers for Simulations of Embryo Growth from 0.1 to 1.0 Myr

Annulus	$a_{\rm in}$ (au)	$a_{\rm out}$ (au)	$N_{\rm part}$
1a	0.48	0.76	4984
1b	0.74	1.02	5106
2a	0.98	1.16	5622
2b	1.14	1.30	5123
2 c	1.28	1.42	3852
2d	1.40	1.54	3758
3a	1.52	1.65	5355

we first separate each annulus into three classes of particles: oligarch embryos (the most massive object in the annulus), protoembryos (all other objects larger than 25 times the initial planetesimal mass), and planetesimals. These class divisions are purely used for our interpolation methodology, and do not affect how the particles are treated in the actual integration. In the intra-annulus regions, we assume that the percentage of total mass concentrated in embryos (both oligarchs and protoembryos) and planetesimals is equal to the arithmetic mean of the corresponding percentages in the neighboring annuli. We then place new oligarch embryos in the region with linearly decreasing masses and semimajor axes that maintain a surface density profile proportional to $r^{-3/2}$. Inclinations and eccentricities for the new oligarch embryos are chosen at random from the original embryo distributions. Finally, we add new protoembryos and planetesimals by randomly drawing masses, eccentricities, and inclinations from the respective distributions, and semimajor axes that maintain $\Sigma_{\rm disk} \propto r^{-3/2}$. Therefore, as radial distance increases in the intra-annulus regions, the total embryo mass is concentrated in a greater number of smaller embryos. All three classes of objects (planetesimals, protoembryos, and embryos) interact with one another gravitationally for this phase of our study.

To verify the effectiveness of our interpolation method, we generate a new artificial, annulus 2 using the outputs of annuli 1 and 3 at $t = 100$ Kyr. When we compare our new artificial annulus with the actual state of annulus 2 at 100 Kyr, we find that the two systems are remarkably similar. Annulus 2 contains 1,378 total particles at this stage of evolution, and our interpolation method creates a system of 1,354 particles. Additionally, our scheme overestimates the mass of the oligarch in annulus 2 by just 3.9%. The ratio of total embryo (oligarchs and protoembryos) to planetesimal mass in the actual annulus 2 is 0.54, as compared to 0.60 in our artificial system. The only manner in which the two systems are significantly dissimilar is in the mass distribution of the protoembryos. Because we are interpolating over such a wide radial range, our artificial system contains around twice as many protoembryos that are, on average, half as massive as those in the real annulus 2. As this issue is lessened when the intra-annulus distance is reduced, we argue that our interpolation prescription is an adequate means for accelerating our calculations while minimizing additional error terms.

Through a process of trial and error, we determine the largest radial bins GENGA can efficiently integrate with fully interacting particles. These seven new, slightly overlapping annuli (Table 2 and Figure 1) are integrated for 900 Kyr using the same gas-disk and boundary conditions described in Section 2.1. Conversely, our two original outermost annuli (2.0 and 3.0 au) are integrated up to $t = 1$ Myr as is.

2.3. *Gas Dispersal and the Influence of Jupiter and Saturn: 1–3 Myr*

At $t = 1$ Myr, we combine all annuli into one large simulation containing 43,608 disk particles using the same interpolation method described in Section 2.2 (however, all objects with $a > 2.0$ au and $M > 25M_{\rm init}$ are treated as protoembryos). Figure 2 plots the radial mass profile of our fully constructed terrestrial formation disk. Because we do not include the $3.0 < r < 4.0$ au region of the disk in any of our $t = 0$–1 Myr integrations given the lengthy timescales for collisions to occur at large radial distances, we approximate this section of the disk in these simulations with planetesimals five times as massive as our initial planetesimals. This region is quickly excited and eroded by perturbations from the giant planets following gas-disk dispersal (e.g., Raymond et al. 2006), therefore we populate the region with unrealistically large asteroids only for the purposes of modeling the exterior mass' effect on the interior disk regions. To further accelerate our calculation, we also treat all planetesimals ($M < 25M_{\rm init}$) as semi-interacting (interact gravitationally with the embryos, but not with one another) for this phase of our study (e.g., Raymond et al. 2009). However, all particles still feel the effects of the decaying gas disk.

At this stage of analysis, we begin to consider the effects of the growing gas giants with three separate models:

1. No giant planets (NOJS)
2. Jupiter and Saturn each with $M = 8.0\ M_\oplus$ (8JS).
3. Jupiter and Saturn begin with $M = 1.0\ M_\oplus$ and grow logarithmically to 95% their modern masses at $t = 3$ Myr (GROW).

In each case, the giant planets are placed on near-circular orbits in mutual 3:2 ($a_{\rm Jup} = 5.6$ au, consistent with the planets' presumed per-instability orbits, see Nesvorný 2011; Deienno et al. 2017) MMR (e.g., Lee & Peale 2002; Clement et al. 2018). We then integrate each system up to $t = 3$ Myr as described above. While none of these giant planet mass configurations are akin to that of the actual solar system, we include them for the purposes of testing, to first order, Jupiter's and Saturn's effect on this phase of terrestrial evolution.

2.4. *The Giant Impact Phase: 3–200 Myr*

While we plan to continue the full-resolution study of our complete terrestrial disk (Figure 2) in a future paper, we present a suite of simplified CPU simulations of the giant impact phase here to briefly comment on the implications of our generated disks. These integrations make use of the *Mercury*6 hybrid integrator (Chambers 1999), employ a 6-day time step, and remove bodies with $r > 100$ au and $r < 0.1$ au. Modern massed versions of Jupiter and Saturn are placed in a 3:2 MMR as described above. All embryos (here $M \geqslant 0.01\ M_\oplus$) from our GENGA simulations are included as fully interacting bodies. The remaining disk mass is replaced by 1000 equal-massed semi-interacting planetesimals with orbits drawn randomly from the remaining GENGA particles such that $\Sigma_{\rm disk} \propto r^{-3/2}$ is maintained. We perform 24 (as these are run on a cluster with 24 CPU cores per node) separate simulations in this manner for our NOJS, 8JS, and GROW disks. Additionally, we completely remove all gas-disk interactions in these simplified integrations. While a step change in the masses of Jupiter and Saturn and gas abundance at $t = 3$ Myr is obviously not realistic, we present

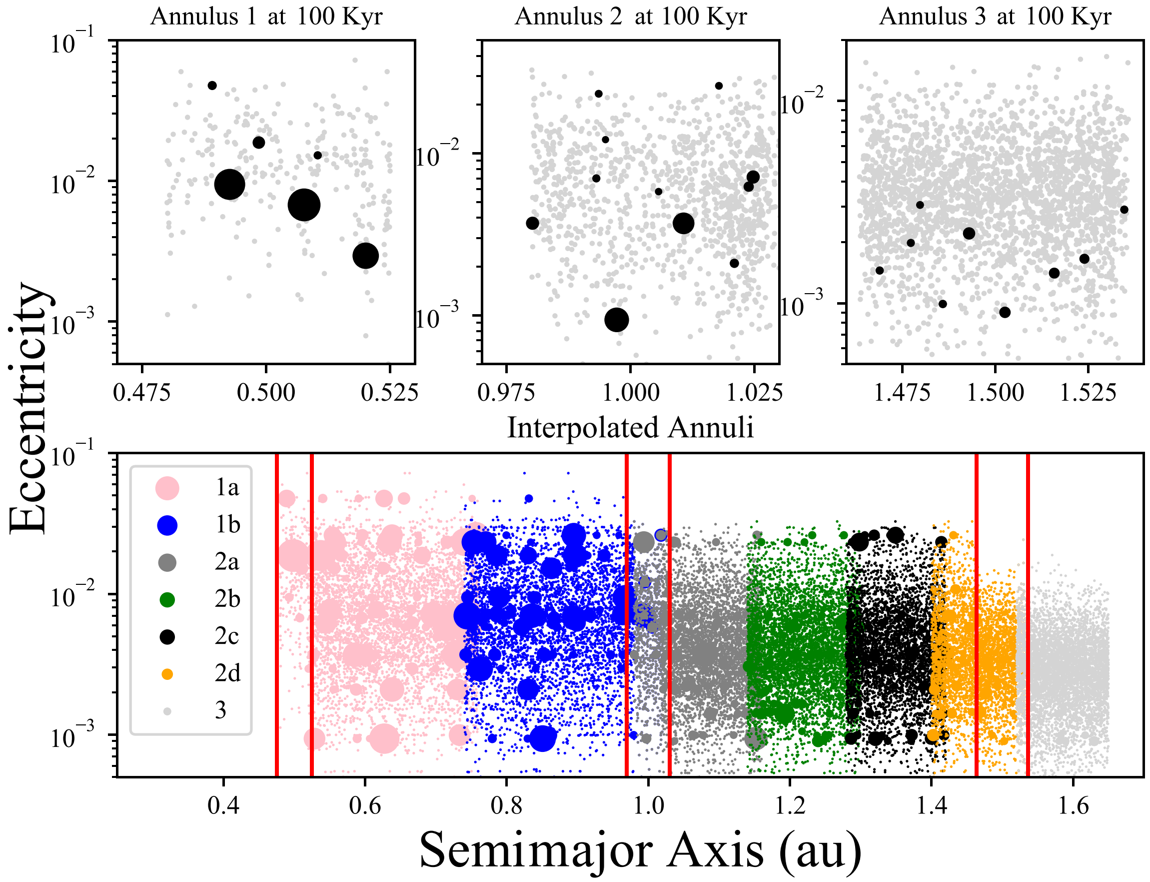

Figure 1. a/e plot of our three innermost annuli (top panels) and seven new interpolated annuli (bottom panel, Table 2) at $t = 100$ Kyr. The edges of the three original initial annuli (1, 2, and 3) from which these new disk conditions are derived are denoted with vertical red lines. The size of each point is scaled to the object's mass, and each color represents a different simulation annuli (by design, the annuli slightly overlap). Note that due to our method of interpolating between annuli (Section 2.2) by drawing from the in situ distribution of orbital elements in the adjacent two annuli, the resulting interpolated particles possess discrete eccentricity values.

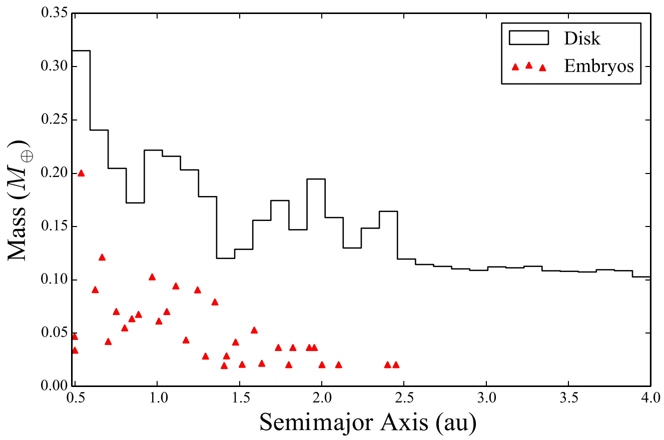

Figure 2. State of the terrestrial disk at 1 Myr; the point where we combine all annuli and add giant planets. At this stage, the system contains 43,608 total disk particles. The state of these systems at $t = 3$ Myr is depicted in Figure 10. The black line represents the total disk mass profile, while the red triangles plot each individual embryo with $M > 0.01\ M_\oplus$.

these simulations here to provide a zeroth-order approximation of the final system architectures.

It should be noted here that the remnant planetesimal population can significantly affect the system's evolution within the giant impact phase (see Raymond et al. 2006, 2007; Jacobson & Morbidelli 2014, where the ratio of total embryo to planetesimal mass is varied). Therefore, our study is inherently biased by our initial planetesimal masses. If the first generation of planetesimals indeed formed large and rapidly (e.g., Morbidelli et al. 2009; Johansen et al. 2015; Dermott et al. 2018), then our $D = 200$ km initial bodies might be realistic. Therefore, we conclude our study with a discussion of how the remnant planetesimal SFD can affect growing embryos with an additional suite of 50 simplified simulations of terrestrial accretion. These simulations are performed with the *Mercury*6 hybrid integrator as described above using embryo and planetesimal distributions similar to those supposed in classic *N*-body studies of terrestrial planet formation (Chambers 2001; Chambers & Wetherill 2001; Raymond et al. 2009). Each simulation assumes a $5M_\oplus$ disk with half its mass concentrated in 50 equal-massed embryos, and the other 50% distributed equally between either 1000 or 2000 planetesimals (25 integrations each). Semimajor axes are selected to achieve $\Sigma_{\text{disk}} \propto r^{-3/2}$, while eccentricities and inclinations are drawn from Rayleigh distributions ($\sigma_e = 0.002$ and $\sigma_i = 0\overset{\circ}{.}2$).

3. Results and Discussion

We present the results of our GPU-accelerated simulations of embryo growth in the subsequent Sections 3.1–3.2. The following Sections 3.3–3.4 discuss the outcomes of our

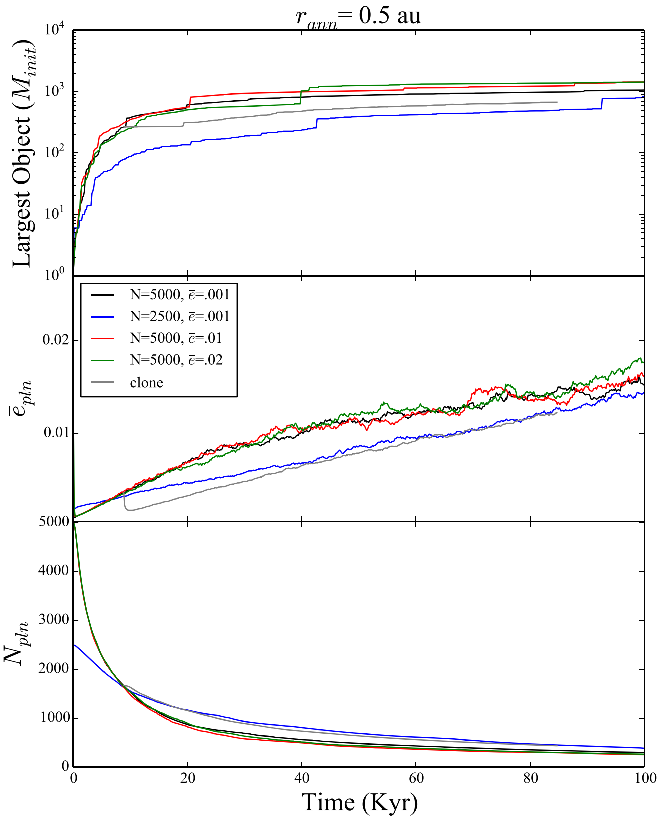

Figure 3. Comparison of varied initial conditions for our $r = 0.5$ au annulus. In the first four runs (color-coded black, blue, red, and green), the initial planetesimal eccentricities and total number of annulus particles are varied. In the final simulation ("clone," gray line), the annulus is tripled in size once the total particle number drops by a factor of three.

additional CPU-only simulations of the giant impact phase of terrestrial planet formation.

3.1. Oligarchic Growth

We begin our analysis with a brief validation of our initial conditions and methods. We perform four additional integrations of our innermost ($r = 0.5$ au) annulus (plotted in Figure 3). In two simulations, we increase the rms eccentricity of our planetesimals ($\bar{e}_{\mathrm{pln}} = 0.01$ and 0.02; red and green lines in Figure 3, respectively) and verify that our results are independent of the particular initial orbits of the planetesimals. Indeed, both simulations experience nearly identical runaway growth sequences. This is because planetesimal orbits are rapidly damped to nearly zero eccentricity at the beginning of our simulations when the gas disk is particularly dense. Next, we perform an integration where the annulus is represented by 2500 equal-massed objects, rather than 5000. While the embryo growth sequence and planetesimal SFD in this run (blue line in Figure 3) are obviously different, we find that the net result at the end of the runaway growth phase is largely the same as in our nominal run in terms of $\bar{e}_{\mathrm{pln}}$ and final embryo mass. Finally, we scrutinize the effectiveness of our boundary condition by tripling the size of our nominal annulus once the total number of particles decreases by a factor of three. This is accomplished by generating two identical exterior annuli where the semimajor axis of each particle is shifted by the annulus width (0.04 au) while holding the other orbital elements constant. The additional dynamical friction of the new surrounding planetesimals has the immediate effect of briefly damping planetesimal eccentricities (gray line in Figure 3), but the net result of the oligarchic growth scheme in terms of M_{iso} and T_{grow} is the same as in our nominal run after 100 Kyr.

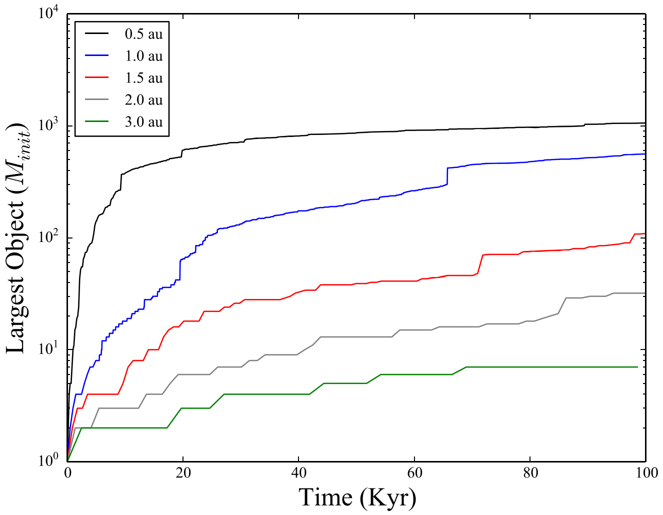

Figure 4. Growth of the largest object in each of our five initial annuli. Oligarchic growth ensues rapidly in the inner disk, while our outermost annulus experiences few accretion events in the first 100 Kyr of evolution.

The mass evolution from $t = 0$–100 Kyr of the largest object in each of our five initial annuli (1–5, Table 1) is plotted in Figure 4. Runaway growth is self-limiting in the sense that it is effectively only dependent on the available mass to be accreted (a function of the local planetesimal surface density and, not considered here, the inward pebble flux) and the rms eccentricity (e.g., Lissauer 1987) in the region as

$$\frac{1}{M}\frac{dM}{dt} \propto \Sigma_{\mathrm{pln}} M^{1/3} \bar{e}_{\mathrm{pln}}^{-2} \tag{2}$$

.

The growth timescale while in the runaway regime is

$$T_{\mathrm{grow}} = \frac{M}{dM/dt}. \tag{3}$$

Taking the "kinetic gas" approach (Wetherill 1980b), and assuming that dM/dt goes as

$$\frac{dM}{dt} = \pi R^2 \rho_{\mathrm{pln}} \bar{v}_{\mathrm{pln}} \left[1 + \left(\frac{v_{\mathrm{esc}}}{\bar{v}_{\mathrm{pln}}}\right)^2\right], \tag{4}$$

(where v_{esc} is the escape velocity at the surface of a growing embryo, ρ_{pln} is the volume density of planetesimals, and $\bar{v}_{\mathrm{pln}}$ is their velocity dispersion), it can be shown that

$$T_{\mathrm{grow}} \simeq 2 \times 10^4 \bar{e}_{\mathrm{pln}}^2 \left(\frac{\Sigma_{\mathrm{pln}}}{\Sigma_o}\right)^{-1} \left(\frac{M}{10^{26}\, g}\right)^{1/3} \left(\frac{a}{1\ \mathrm{au}}\right)^2 \mathrm{y}. \tag{5}$$

Here $\Sigma_o = 10$ g cm^{-2} at 1 au (see Kokubo & Ida 1995, for a full derivation). Note that here, the rms planetesimal eccentricity is scaled by the reduced Hill radius,

$$h_r = \left(\frac{M}{3M_{\odot}}\right)^{1/3}. \tag{6}$$

The runaway-growth regime is only relevant when Σ_{pln} is large and ample planetesimals are available to feed the growing

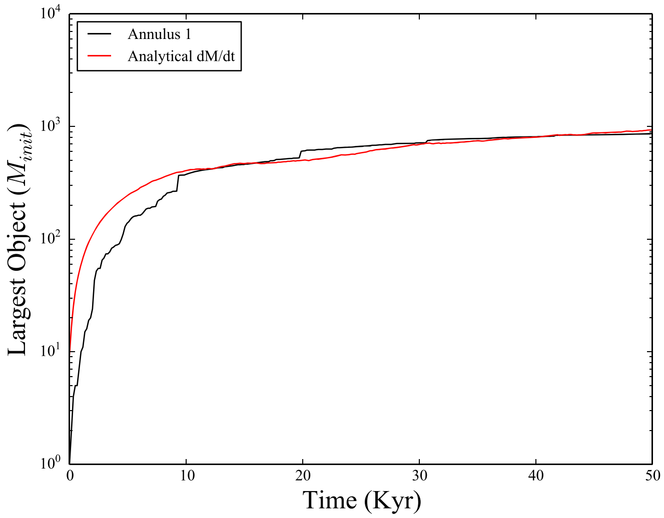

Figure 5. The same as Figure 4 for annulus 1, compared with analytical dM/dt (Equation (5)) using the in situ values of $\Sigma_{\rm pln}$, M, and $\bar{e}$. As $T_{\rm grow} \ll \tau_{\rm gas}$ in annulus 1, accretion is rapid and well characterized by the runaway growth regime.

embryo. Therefore, this relationship of Equation (5) is typically cited in reference to growth toward the "isolation mass" (e.g., Kokubo & Ida 2002; Kobayashi & Dauphas 2013),

$$M_{\rm iso} = 0.14\chi^{3/2}\left(\frac{a}{1.5\ {\rm au}}\right)^{3/4} \qquad (7)$$

,where χ is the scaling of the classic Hayashi (1981) MMSN. For $\chi = 1$, this relationship predicts Mars-massed embryos accreting at ∼1.5 au, and larger embryos in the asteroid belt region. In practice, however, the isolation mass is likely never reached in the outer terrestrial disk because the timescales for giant planet growth and gas dispersal are significantly shorter than $T_{\rm grow}$ for $a \gtrsim 1.5$ au. Thus, other dynamical processes likely begin perturbing this region long before $M_{\rm iso}$ is reached. In contrast to the outer disk, accretion in our innermost annuli is indicative of runaway growth (Equation (5) and Figure 5. For our purposes, however, we are most interested in the time required to accrete embryos of different masses because we seek to infer the conditions of the terrestrial disk around the time of nebular gas dispersal. Figure 6 depicts this relationship for our five annuli for two different growth masses. Assuming no evolution in $\bar{e}^2_{\rm pln}$, from Equation (5), we would expect $T_{\rm grow}$ in our $\Sigma \propto r^{-3/2}$ disk to scale as a^2 with increasing radial distance. In our simulations, however, we find that it scales closer to $\sim a^3$. Additionally, growth toward higher masses (bottom panel of Figure 6) is further curtailed in the outermost annulus and better fit by an $\sim a^{3.5}$ radial dependency. These results are largely consistent with previous studies (Kokubo & Ida 2002; Chambers 2006; Kobayashi & Dauphas 2013) and analytical derivations incorporating the radial dependencies of $\bar{e}_{\rm pln}$ (mainly a result of gas dynamics) and the isolation mass (e.g., Kokubo & Ida 2002, infer an $a^{2.7}$ dependency). In a recent study similar to our current work, Walsh & Levison (2019) report that $T_{\rm grow}$ toward $M_{\rm iso}$ scales as $\sim a^{3.6}$ in nominal MMSN models without collisional grinding. Because $M_{\rm iso}$, increases with radial distance (Equation (6)), our measured times to reach a fixed embryo mass in different radial annuli are indicative of an even steeper scaling of $T_{\rm grow}$ with a, particularly in our outermost annulus. This is at least partially a result of our inclusion of the giant planets in two of our 1–3 Myr simulations. While Figure 6 plots the time to reach $M = M_{\rm moon}$ for annulus 5 (Table 1) as the average of all three simulations, we note that this time is ∼600 Kyr shorter in our NOJS run than in our other two runs. Thus, perturbations from the growing giant planets, though significantly damped in the gas-disk phase, are still sufficient to moderately excite orbits and limit accretion events in the asteroid belt region.

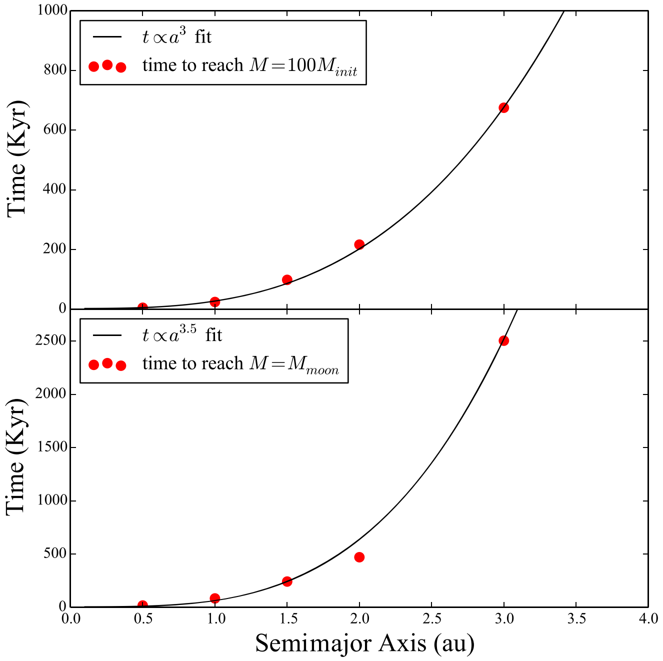

Figure 6. The time required for a planetesimal to increase in mass by two orders of magnitude (top panel) and the time to accrete a Moon-massed embryo (bottom panel) for each of our five annuli.

Table 3
Ratios of Total Embryo Mass to Total Planetesimal Masses (R) in Different Disk Regions after 3 Myr of Evolution for Our Three Different Simulations

Run	$R(a < 1$ au)	$R(1 < a < 2$ au)	$R(2 < a < 3$ au)
NOJS	3.33	1.76	0.28
8JS	3.81	1.56	0.22
GROW	2.95	2.16	0.25

3.2. Initial Conditions after Nebular Gas Dissipation

Our three runs (NOJS, 8JS, and GROW) finish with an average total terrestrial disk mass of 4.3 $M_\oplus$. In general, our simulations predict ∼0.3 $M_\oplus$ embryos forming at $a < 1.0$ au, Mars-massed objects accreting in the proto-Mars region, and several small Moon-massed embryos growing in the inner asteroid belt region (see Figures 8 and 10). However, we find that the belt region is totally dominated by smaller planetesimals, rather than embryos, at this phase of evolution. Objects similar in mass to Ceres are quite prevalent throughout the asteroid belt (an average of 571 objects with $M_{\rm Ceres} < M < 10M_{\rm Ceres}$), while each system contains only ~5 larger embryos of about lunar mass (>0.01 $M_\oplus$). Table 3 summarizes the ratio (R) of embryo ($M > 0.01\ M_\oplus$) to planetesimal mass at different locations within the terrestrial disk at $t = 3$ Myr. The disparity between our generated R values throughout the disk and assumptions of N-body studies (Chambers 2001; Raymond et al. 2009; Clement et al. 2018) is an important takeaway from our simulations because different bimodal make-ups can lead to different evolutionary outcomes in different radial regions. We address each zone individually in the following sections.

3.2.1. Inner Disk

The innermost sections of our disks, where $M_{\rm iso}$ is approached rapidly, are heavily depleted of planetesimals at $t = 3$ Myr. This can have significant implications on the follow-on evolution of Earth and Venus analogs within the giant impact phase. In general, higher R values lead to less dynamical friction generated by planetesimals. Because swarms of planetesimals can damp the orbits of the growing planets (discussed further in Section 3.4), this can result in final systems of planets with unrealistically high eccentricities and inclinations. However, Lykawka & Ito (2019) analyzed terrestrial growth within various evolutionary schemes using initial values of $R = 1$, 4, and 8. The authors noted that high-R disks were typically more successful at yielding small-Mars analogs, replicating late veneer accretion on the Earth, and generating Mercury-Venus pairs. Furthermore, Jacobson & Morbidelli (2014) found that employing a high-R disk was an effective mechanism for delaying the Moon-forming impact and thus providing an adequate match to the amount of material delivered to form the late veneer. Therefore, a high-R disk would be advantageous if another mechanism were capable of limiting the eccentricities and inclinations of Earth and Venus.

3.2.2. Mars Region

In the Mars region, slightly elevated R values ($R \simeq 2.0$ as opposed to $R = 1.0$ that is often assumed in the literature: Chambers 2001; Raymond et al. 2009; Clement et al. 2018) can potentially alter final system outcome within an early Nice Model evolutionary scheme. Clement et al. (2018) argued that instabilities timed ~1–10 Myr after nebular gas dispersal are most successful at limiting Mars' mass (compared with earlier instabilities) because the higher R values achieved at more advanced evolutionary stages lead to levels of dynamical friction that are insufficient to save material from loss during the instability. Therefore, in an early instability scenario, the higher values of R in the Mars region (Table 3) of our simulations might lead to greater mass loss (Clement et al. 2019c) and improved outcomes in a scenario where the giant planet instability is the Mars mass-depletion event. Moreover, Lykawka & Ito (2019) found that higher-R disks ($R = 4$ or 8, as opposed to $R = 1$) were about twice as likely to produce a Mars analog with the correct mass and orbital offset from Earth.

3.2.3. Asteroid Belt

Consistent with Equation (5), the primordial asteroid belt planetesimals are relatively unprocessed at $t = 3$ Myr. This is slightly more pronounced in our simulations that include the giant planets (however, we find this trend to be weak and inconclusive; Table 3). While we would expect our results in the inner disk to be somewhat independent of our selection of initial planetesimal mass (as $T_{\rm grow} \lesssim \tau_{\rm gas}$), our asteroid belt results are significantly biased by our initial conditions. Thus, as accretion events in the asteroid belt are rare in our simulations, our selected primordial asteroid sizes are strongly preserved in the final SFD. While it should be noted that we do not test this hypothesis by varying $M_{\rm init}$, if the initial asteroids indeed formed large (Morbidelli et al. 2009; Johansen et al. 2015; Dermott et al. 2018), our results indicate that the region would be dominated by a few asteroids of lunar mass, and dozens of Ceres-massed objects when the nebular gas dissipated. However, it should be noted that these results are specific to our assumption of a "heavy" primordial belt and a uniform $\Sigma \propto r^{-3/2}$ disk (see, e.g., Izidoro et al. 2014, 2015, for an analysis of different disk profiles).

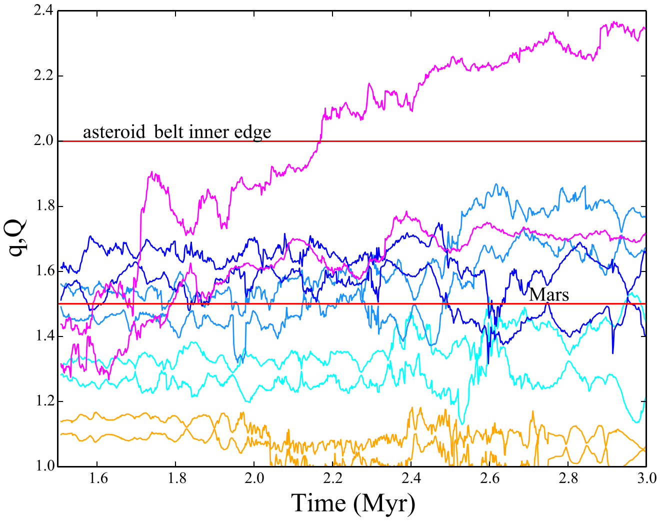

Figure 7. Perihelia and aphelia vs. time for three growing embryos in the Mars region (plotted in different shades of blue; each begins with a mass between that of the Moon and Mercury at $t = 1.0$ Myr, and grows to about one Mars mass at $t = 3.0$ Myr) interacting with and scattering a small planetesimal (pink line) into the asteroid belt. The proto-Earth embryo is plotted in orange. The horizontal red lines correspond to the modern semimajor axes of Mars and the asteroid belt's inner edge.

Planetesimals are occasionally implanted into the belt from the inner disk regions in our simulations. The largest radial migration of a Ceres-massed asteroid from $t = 1$–3 Myr in any of our simulations is ~1.1 au, and each system implants an average of $\sim 10^{-4} M_{\oplus}$ worth of material originating with $a < 1.5$ au in the belt. Therefore, if Vesta had formed in the inner terrestrial region (as suggested by its composition; Bottke et al. 2006; Mastrobuono-Battisti & Perets 2017), our results imply that its implantation in the belt could have occurred during the gas-disk phase of evolution (however, the scarcity of such events in our simulations would indicate that this is unlikely given the subsequent depletion of the belt; O'Brien et al. 2007; Clement et al. 2019c). An example of this type of planetesimal scattering from our GROW simulation is plotted in Figure 7. In that run, a small planetesimal originating at $a = 1.38$ au experiences a series of close encounters with three large embryos in the proto-Mars region that drive its aphelion well into the asteroid belt. While the planetesimal's orbit still crosses that of one of three embryos at $t = 3$ Myr, it is possible that it could be further scattered onto a stable orbit in the asteroid belt during the giant impact phase (e.g., Sandine & Jacobson 2019).

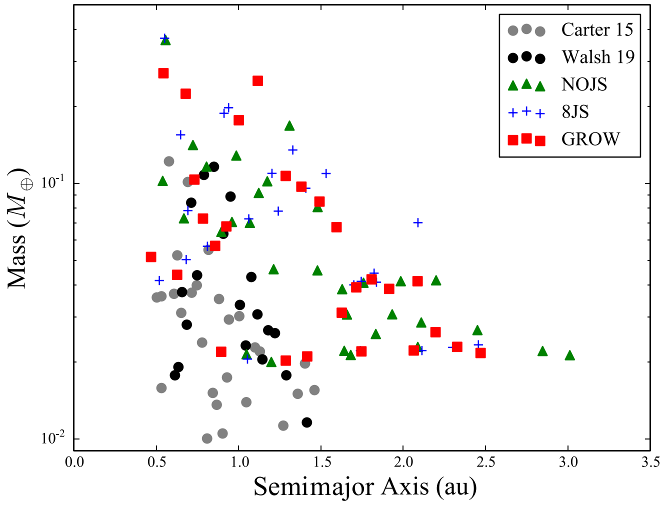

Figure 8. Embryo (only objects with $M > 0.01M_\oplus$ are plotted) distributions at $t = 2$ Myr for our three different simulations compared with results from Carter et al. (2015) and Walsh & Levison (2019; gray and black circles, respectively).

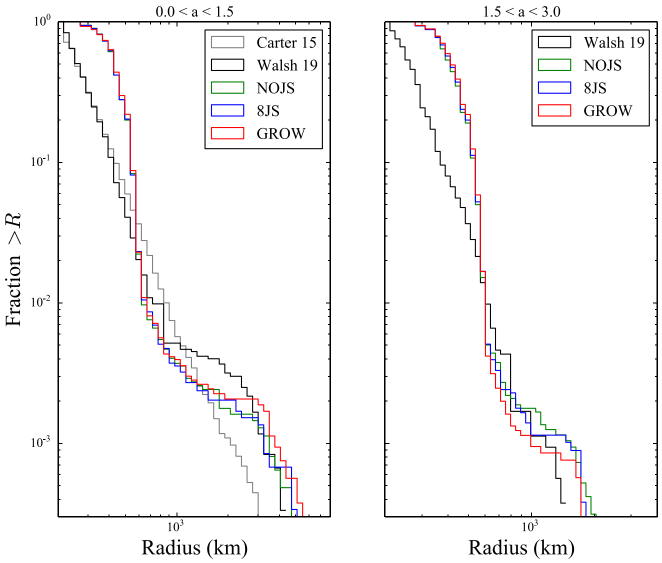

Figure 9. SFD at $t = 2$ Myr for the inner ($a < 1.5$ au, left panel) and outer ($1.5 < a < 3.0$ au, right panel) regions of the terrestrial disk, compared with results from Carter et al. (2015) and Walsh & Levison (2019; gray and black lines, respectively).

3.2.4. Comparison with Previous Work

We compare the state of our terrestrial disk at $t = 2$ Myr with previous work by Carter et al. (2015) and Walsh & Levison (2019) in Figures 8 and 9. In both figures, we consider the results of each paper's nominal MMSN calculations (using the nomenclature of Carter et al. 2015, this is the high-resolution calm disk). For reference, the simulation from Carter et al. (2015) does not include the giant planets, while Walsh & Levison (2019) place 1 $M_\oplus$ versions of Jupiter and Saturn at $a = 3.5$ and 6.0 au that are instantaneously moved to their modern masses and preinstability orbits ($a = 5.0$ and 9.2 au: Levison et al. 2011) at $t = 4.0$ Myr. Additionally, the simulation of Carter et al. (2015) begins with $D = 196$–1530 km planetesimals drawn from an SFD power law of $dN = m^{-2.5}dm$ and simplifies collisions by inflating radii by a factor of 6. In contrast, Walsh & Levison (2019) use initial planetesimals drawn from a distribution centered around $r = 30$ km. Because our simulations begin with $D \simeq 200$ km equal-massed planetesimals, it is not surprising that our final SFDs (Figure 9) are relatively steep, with a tail superimposed by runaway growth.

We note significant differences between our results and those of the two previous studies. Three main factors contribute to these disparities: our wider initial planetesimal disk, our intra-annulus interpolation method, and our direct treatment of collisions and close encounters without collisional fragmentation. While Carter et al. (2015) and Walsh & Levison (2019) study more narrow disk regions (0.5–1.5 and 0.7–3.0 au, respectively), our work considers the entire radial range of 0.48–4.0 au (Table 2). Perhaps the largest difference between our respective final embryo distributions (plotted in Figure 8) is the prevalence of Moon- to Mars-massed embryos in the 1.5–2.0 au region, and Moon-massed embryos in the inner asteroid belt in our simulations. These differences are mostly a result of our larger initial planetesimals. Nominal simulations in Walsh & Levison (2019) begin with $r \simeq 15$ km planetesimals placed throughout the disk. Because 2 Myr is significantly shorter than T_{grow} at $a > 2.0$ au, our results are more biased by the larger planetesimal sizes than they are by the outcomes of runaway growth. This is further evidenced by low R values in the asteroid belt in our simulations. The difference in initial planetesimal sizes is also fossilized in our final SFDs (Figure 9), thus resulting in an overabundance of ∼100–500 km planetesimals compared with Carter et al. (2015) and Walsh & Levison (2019).

In general, our final SFDs are significantly more indicative of runaway growth than are those of Carter et al. (2015) and Walsh & Levison (2019). We speculate that this is a result of our treatment of collisions and close encounters (without inflating planetary radii or using tracer particles). Thus, once the total planetesimal number decreases, growing embryos in our simulations begin to both gravitationally focus smaller planetesimals onto collision courses and heat up the local velocity dispersion through scattering events.

Our method of interpolating between annuli likely artificially accelerates growth, and we find this effect to be most consequential in the $0.5 < a < 1.0$ region. When we begin to interpolate at $t = 100$ Kyr, the oligarch embryo in the annulus 1 ($r = 0.5$ au) is about five times larger than the oligarch of annulus 2 ($r = 1.0$ au). Because we linearly interpolate between these regions when laying new oligarch embryos (rather than logarithmically), embryos in the middle of the intra-annulus regions are boosted in mass (relative to those of, e.g., Walsh & Levison 2019). Because this is also true for annuli 2 and 3, this has the cumulative effect of boosting the total mass concentrated in embryos in the inner terrestrial disk relative to those of Carter et al. (2015) and Walsh & Levison (2019).

Carter et al. (2015) and Walsh & Levison (2019) each incorporate algorithms designed to account for the effects of collisional fragmentation by introducing new "fragment" particles (or tracers) when imperfect collisions occur (e.g., Leinhardt & Stewart 2012; Stewart & Leinhardt 2012). Conversely, our work treats all collisions as perfectly accretionary. It is difficult to assess the degree to which our results differ from those of models considering collisional fragmentation without a consistent set of control runs. It is also unclear whether collisional fragmentation plays a significant role in altering the final distribution of embryo masses because

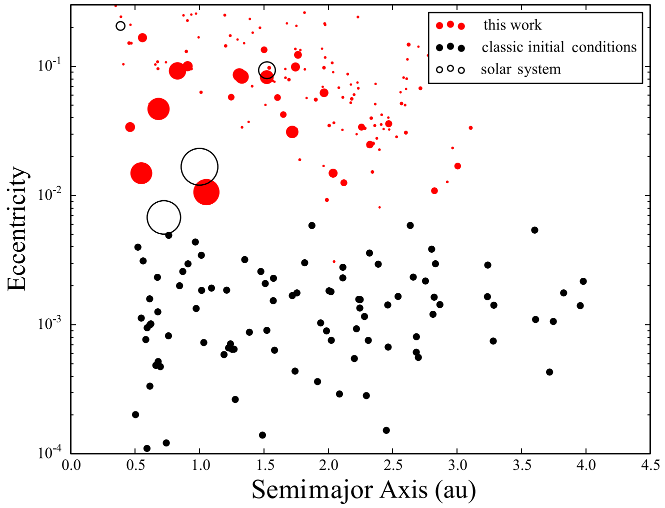

Figure 10. Comparison of all objects with $M > 0.001M_\oplus$ in our GROW simulation (red dots) with a typical distribution of 100 equal-massed embryos used in N-body studies (black dots, e.g., Chambers 2001; O'Brien et al. 2006; Clement et al. 2018) and the modern terrestrial planets (open circles). The size of each point is proportional to the object's mass.

generated fragment particles can obviously be reaccreted later in the simulation, thus lengthening the accretion timescale while resulting in a similar final system architecture. Indeed, Deienno et al. (2019) concluded that energy dissipation occurring during fragmenting, embryo-embryo collisions do not contribute to significant differences of final system structure in terrestrial planet formation (both in terms of orbital excitation and planet mass). However, other authors using different numerical implementations have reached the opposite conclusion (e.g., Bonsor et al. 2015; Clement et al. 2019b; Kobayashi et al. 2019). Thus, one could argue that the results of computational investigations of fragmentation are dependent on the specific numerical approach taken (and therefore more sophisticated models are required to study the problem). While a complete analysis of imperfect accretion is beyond the scope of this work, we cannot discount collisional fragmentation as a potential contributor to the observed differences in embryo masses and planetesimal SFDs in Figures 8 and 9. Therefore, growth toward higher embryo masses is potentially artificially accelerated in our simulations compared to those of Carter et al. (2015) and Walsh & Levison (2019; the degree to which this might hold is unclear).

We also note that our disk populations are significantly more bimodal in mass than those in Carter et al. (2015). At first glance, this seems to imply that our simulations are significantly further evolved within the runaway growth phase. However, simulations in Carter et al. (2015) begin with planetesimal sizes ranging from 196 to 1530 km in order to resemble a more advanced stage of oligarchic growth. Thus, this range of primordial sizes seems to persist in the simulations of Carter et al. (2015) through the $t = 2$ Myr point. Therefore, the differences between our respective SFDs can be interpreted as a fossilization of the initial planetesimal population. In Section 3.4 we speculate further about how this fossilized initial planetesimal distribution might effect the giant impact phase.

Table 4
Summary of Various Statistics for Our Different Batches of Simulations Designed to Study the Giant Impact Phase of Terrestrial Planet Formation (NOJS, 8JS, GROW, and Classic (Chambers 2001) Initial Conditions with Either 1000 or 2000 Equal-massed Planetesimals)

Set	N_{TP}	AMD/AMD$_{\mathrm{SS}}$	RMC/RMC$_{\mathrm{SS}}$	M_{Mars}
NOJS	5.1	0.73	0.29	0.63
8JS	6.4	0.55	0.29	0.40
GROW	5.5	1.04	0.28	0.60
Classic, 1000	4.4	5.6	0.41	0.76
Classic, 2000	4.3	5.8	0.37	0.43

The columns are as follows: (1) the simulation set (each made up of 24 separate integrations), (2) the mean total number of terrestrial planets ($a < 2.0$ au, $m > 0.05\ M_\oplus$) after 200 Myr, (3) the mean normalized AMD (Equation (8)), (4) the mean normalized RMC (Equation (9)), and (5) the mean Mars-analog mass (in Earth units, defined here simply as the largest planet with $1.3 < a < 2.0$ au; Clement et al. 2018).

3.2.5. New Distributions for Giant Impact Studies

In Figure 10 we plot the state of our GROW simulation at $t = 3$ Myr, compared with initial conditions that are typically used in simulations of the giant impact phase (e.g., Chambers 2001). In our simulations, the inner disk ($r \lesssim 1.5$ au) attains quite an advanced evolutionary state prior to nebular gas dispersal, and the system already resembles some aspects of the modern terrestrial architecture. In fact, the largest two embryos in our 8JS simulation (a proto-Venus analog at $a = 0.6$ au and a proto-Earth at $a = 0.9$ au) each possess masses of 0.39 $M_\oplus$. The consequences of such a distribution of embryos for the post-gas-disk phase of giant impacts is obvious. As described in Walsh & Levison (2019; we expand upon this further in Section 3.3), the ultimate phase of terrestrial assembly proceeds as a late instability. Thus, rather than about one hundred embryos accreting over hundreds of giant impacts, around a dozen embryos experience just a handful of massive impacts as they continue to accrete small bodies over hundreds of million years. Furthermore, such an evolutionary scheme might be consistent with planetary differentiation models (Rubie et al. 2015) that suggest that Venus' lack of an internally generated magnetic dynamo implies that primordial stratification in its core was never disrupted and mixed by a late giant impact (Jacobson et al. 2017).

3.3. Fully Evolved Systems

For a first-order approximation of the evolution of our $t = 3$ Myr systems up to $t = 200$ Myr, we perform an additional suite of simplified CPU integrations where the planetesimal population is approximated with 1000 equal-massed objects. We provide a summary of important statistics for each set of runs in Table 4 (commonly cited as "success criteria" for terrestrial planet formation models; see, e.g., Raymond et al. 2009; Clement et al. 2018; Izidoro & Raymond 2018). The evolution of these systems within the giant impact phase is strikingly different from that of the "classic" model for terrestrial planet formation (e.g., Wetherill 1980b; Chambers 2001). Most notably, our new distributions of large ~0.1–0.4 $M_\oplus$ embryos struggle to combine into systems of four larger terrestrial planets. The largest embryos accrete the remaining planetesimals (as well as the occasional smaller embryo), but the embryo systems seldom destabilize fully and experience a final series of giant

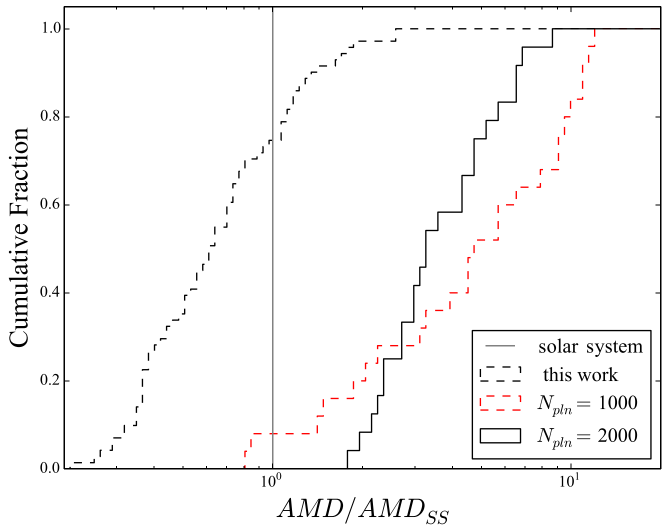

Figure 11. Cumulative distribution of normalized AMDs (Equation (8)) for three separate batches of terrestrial planet formation simulations. The black lines plot simulations that employ “classic” initial conditions (e.g., Chambers 2001; O’Brien et al. 2006; Clement et al. 2018) where half of the disk mass is placed in 50 equal-massed embryos and either 1000 (solid line) or 2000 (dashed line) equal-massed planetesimals. The red line depicts the results of 72 simulations using embryo distributions generated from the GPU simulations presented in this work. The vertical gray line denotes the solar system AMD for Mercury, Venus, Earth, and Mars.

impacts with one another. Thus, the resulting systems contain too many terrestrial planets that are systematically undermassed. Indeed, the mean number of planets with $a < 2.0$ au and $m > 0.05\ M_{\oplus}$ in our 8JS simulations using new initial conditions is 6.4, as opposed to 4.3 in our simulations that employ “classic” initial conditions (discussed further in Section 3.4). Furthermore, because our new systems evolve only slightly over 200 Myr, the final terrestrial planets largely maintain the dynamically cold orbits that were originally damped via interactions with the gas disk. To demonstrate this, we calculate the normalized angular momentum deficit (AMD; Laskar 1997) and radial mass concentration statistics (RMC: Chambers 2001) for each system,

$$\mathrm{AMD} = \frac{\sum_i M_i \sqrt{a_i}\,[1 - \sqrt{(1 - e_i^2)}\cos i_i]}{\sum_i M_i \sqrt{a_i}}, \tag{8}$$

$$\mathrm{RMC} = \mathrm{MAX}\left(\frac{\sum_i m_i}{\sum_i m_i \left[\log_{10}\left(\frac{a}{a_i}\right)\right]^2}\right). \tag{9}$$

Figure 11 plots the cumulative distribution of system AMDs for our 72 simulations that are based on the results of our GPU simulations, compared with 50 control simulations that make use of classic initial conditions. Given the limited number of large accretion events experienced in our GPU-derived simulations, the final terrestrial architectures consistently provide better matches to the actual inner solar system in terms of system AMD. We hesitate to conclude that this result implies a potential solution to the terrestrial overexcitation problem given the poor solar system analogs produced by our integrations. Specifically, we consistently form undermassed Earth and Venus analogs that are too great in number, and overmassed Mars analogs that are also overabundant. Nevertheless, the result of final system AMD being limited in systems where embryos attain a more advanced evolutionary state in the gas phase is intriguing and is an avenue for future development and study.

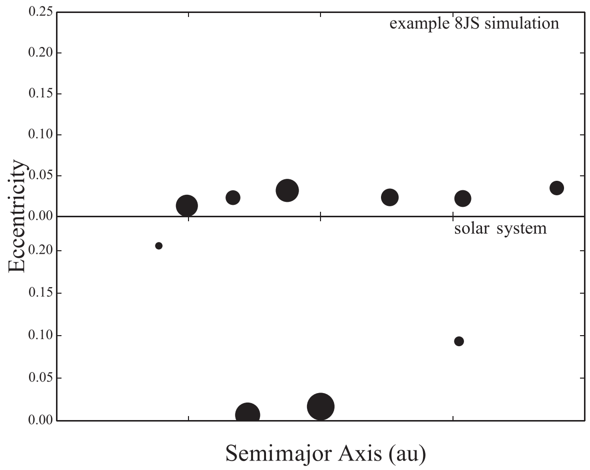

Figure 12. An example final terrestrial system from the 8JS batch (note that this example is chosen specifically to highlight the failure of this model). In order of increasing semimajor axis, the six terrestrial planets in the system have masses of 0.62, 0.26, 0.69, 0.38, 0.35, and 0.25 $M_{\oplus}$.

At first glance, it would appear that the reason for the stunted growth of our systems of larger embryos is the presence of compact MMR chains that develop as a result of aerodynamic-drag-induced migration during the gas-disk phase (a less extreme version of the “breaking of chains” model for compact systems of super-Earths described in Izidoro et al. 2017). Indeed, many of the large embryos in our GPU simulations finish near the major first-order MMRs. As an example, the seven largest embryos with $a < 2.0$ au in our GROW simulation lie just outside of a mutual 3:2,3:2,5:3,4:3,4:3,4:3 chain. However, on closer inspection, these protoplanets are not in resonance, nor do they fall into resonance during the giant impact phase. Instead, the dearth of massive accretion events in these simulations can be attributed to the high R values in the inner disk, in conjunction with a relatively wide spacing between embryos (as opposed to, e.g., Kokubo & Ida 2000). Because the large embryos emerge from the gas disk on low eccentricity orbits well outside one another’s mutual Hill spheres, with very little planetesimal mass available to perturb them on to crossing orbits, these systems routinely remain stable for 200 Myr. An example of such a system from the 8JS set is plotted in Figure 12. Given the modern eccentricities of Mercury ($e = 0.21$) and Mars ($e = 0.09$), the degree of orbital excitation in this system is remarkably low, and this is a typical outcome of our study. However, Earth and Venus only attain ∼70% of their modern masses, and four additional planets with two to three times the mass of Mars are stable in the system (one in the region between Earth and Venus, and three in the Mars region).

The total mass of planets in the Mars region (as well as that of the largest Mars analog; Table 4) is clearly too high in our simulations. However, this is somewhat expected given that our systems grow from a uniform 5 $M_{\oplus}$ disk of material. Thus, we do not account for early depletion in the Mars-forming and asteroid belt regions that might have resulted from giant planet migration (Walsh et al. 2011) or a primordial gap (Raymond & Izidoro 2017), nor do we consider the dynamical excitation of the giant planets (which is highly efficient at limiting the mass of Mars, e.g., Raymond et al. 2009; Lykawka & Ito 2013; Bromley & Kenyon 2017). Nevertheless, it is obvious that if the Earth and Venus analogs in Figure 12 each accreted one of the additional ~0.2–0.3 $M_\oplus$ embryos, perhaps ejecting an additional Mars analog in the process, the final system would provide a much better match to the modern Venus–Earth–Mars architecture.

3.3.1. Implications for the Moon-forming Impact

It follows naturally to speculate that given our results, a dynamical trigger might be required to destabilize such a compact system terrestrial embryos, eject additional Mars analogs, form the Moon, and complete terrestrial planet formation. The logical trigger would be the giant planet instability (Tsiganis et al. 2005; Levison et al. 2008; Deienno et al. 2017). Several recent authors have invoked an early instability rather than a "delayed" instability coincident with the Late Heavy Bombardment (Tera et al. 1974; Gomes et al. 2005). Morbidelli et al. (2018) argued that because the crystallization of the Moon's mantle took longer than that of the Earth's, sequestration of highly siderophile elements (HSEs) during the crystalization process can explain the observed Earth–Moon HSE disparity, and is consistent with an early instability. Indeed, the early impact chronology on the Moon and Mars appears consistent with an instability occurring within 100 Myr of the solar system's birth (Mojzsis et al. 2019; Brasser et al. 2020) Additionally, Nesvorný et al. (2018) showed that the instability must have occurred within 100 Myr of nebular gas dispersal in order to permit the survival of the Patroclus-Menoetius binary system of Jupiter Trojans. Furthermore, a delayed dynamical event in the outer solar system is at odds with the recently discovered asteroid families by Delbo' et al. (2017) and Delbo et al. (2019) in the inner main belt that are inferred to be as old as the solar system (e.g., Milani et al. 2017). Finally, an early instability is also capable of limiting Mars' accretion (Clement et al. 2018), and adequately exciting (Deienno et al. 2018) and depleting (Clement et al. 2019c) the asteroid belt. However, Clement et al. (2019b) require a very specific timing for the instability (1–5 Myr after gas dissipation) to limit Mars' mass and prevent the terrestrial disk from "respreading" and forming 3–4 equal-massed planets (however, this issue might be less pronounced in a higher-R disk, see the discussion in Section 3.2). Imposing such a strict constraint on the instability occurrence is problematic in that it contradicts recent studies of Neptune's effect on the Kuiper Belt (Nesvorný & Vokrouhlický 2016) that aim to explain the inclination distribution of the 3:2 MMR population (Nesvorný 2015a). Specifically, Nesvorný (2015b) requires that Neptune migrate smoothly for ~20 Myr before experiencing a "jump" in semimajor axis (though recent work by Volk & Malhotra 2019 suggests that other timescales are also viable). Thus, we propose that assuming more realistic initial distributions of embryos in the terrestrial forming disk (as produced via our high-resolution GPU simulations) might provide greater flexibility in terms of the timing of the giant planet instability for the early instability scenario proposed in Clement et al. (2018). Indeed, we find that Mars analogs already have masses of about 0.1 $M_\oplus$ after the gas-disk phase (Figure 3). In several of our simulations of the giant impact phase, many Mars analogs do not grow larger beyond the ~10% level over 200 Myr (31% of the planets in the region accrete no additional embryos after $t = 10$ Myr). Thus, it seems reasonable, given our simulation results, that a system of 4–5 Mars-massed planets formed during the gas-disk phase (consistent with the hypothesis that Mars is a "stranded embryo" given its rapid inferred accretion timescale; Dauphas & Pourmand 2011; Kruijer et al. 2017) could remain stable for some tens of million years before it is disrupted by the giant planet instability.

Our generated embryo configurations also imply a mass ratio between the proto-Earth and the Moon-forming impactor (Theia) closer to unity. This result is interesting given that a giant impact involving two ~0.5 $M_\oplus$ bodies has been shown to be successful at replicating the observed isotope ratios (Canup 2012). Kaib & Cowan (2015) found these conditions to be highly improbable within dynamical simulations of terrestrial planet formation that invoke classic (Chambers 2001) initial conditions. While beyond the scope of our present manuscript, the implications of our GPU-evolved embryo populations are nonetheless intriguing with respect to the Moon's formation.

In summary, the results of our simplified simulations that follow the evolution of our GPU-generated embryo distributions within the giant impact phase lead us to speculate that an alternate evolutionary sequence might have ensued during the ultimate phase of terrestrial assembly in the solar system. However, given the simplicity of the numerical simulations presented in this paper, we leave the full development of this scenario to future work. In short, our results indicate that the giant impact phase might have played out as a delayed instability, as proposed in a similar study by Walsh & Levison (2019). This starkly contradicts the rather prolonged sequence of hundreds of giant impacts that is modeled throughout much of the literature (e.g., O'Brien et al. 2006; Fischer & Ciesla 2014; Lykawka & Ito 2019). Because the interior regions of our terrestrial disks achieve extremely high R values and possess well-spaced orbital configurations during the nebular gas phase, we propose that a dynamical trigger such as the Nice Model instability is necessary to stimulate the destabilization of the primordial protoplanets in the inner solar system. In such a scenario, the instability would have to be responsible for both triggering the final few giant impacts on Earth and Venus (most importantly, the Moon-forming impact, e.g., Kaib & Cowan 2015; Quarles & Lissauer 2015) and evacuating the ~1.3–2.0 au region of additional Mars-massed planets (Clement et al. 2018).

3.4. Dependency on Planetesimal Sizes

Left behind after the processes of embryo formation and oligarchic growth is a remnant of the initial planetesimal size distribution. While understanding the properties of the first generation of planetesimals is still an area of active research (e.g., Levison et al. 2015; Drażkowska et al. 2016; Wallace et al. 2017), we argue that the SFD of the residual planetesimals can influence the final system AMDs. As a protoplanet grows within a swarm of smaller planetesimals, it undergoes a constant series of close encounters that tend to reduce the system's AMD. Thus, the e/i evolution of a growing planet in a planetesimal disk can be thought of as a random walk of encounters with a net trend toward damping the planet's orbit. It follows that with a smaller number of larger planetesimals, it is possible to randomly walk toward lower vales of e/i and smaller AMDs. We demonstrate this concept in Figure 13 with a simple numerical experiment using *Mercury* (Chambers 1999). In each simulation, we embed a 1 $M_\oplus$ planet

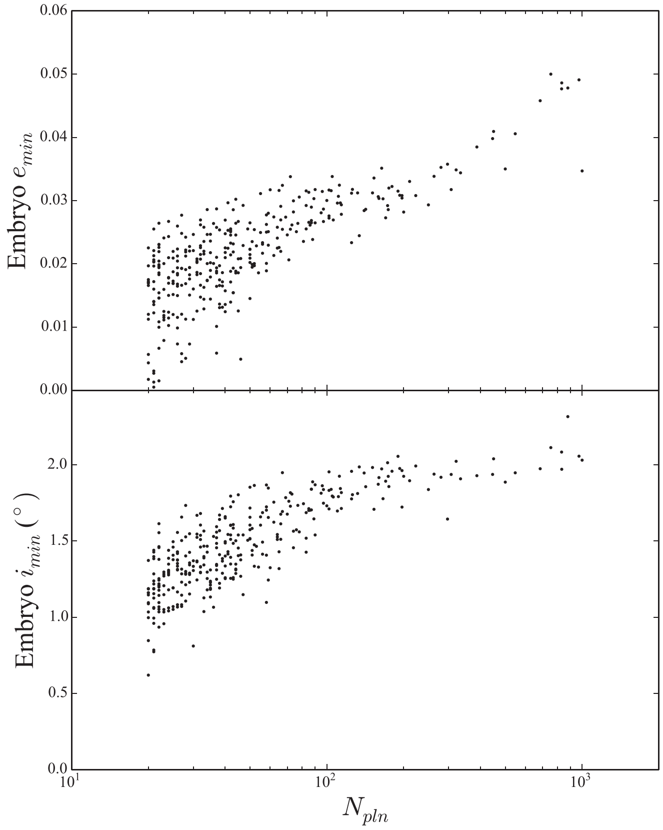

Figure 13. Minimum eccentricity (top panel) and inclination (bottom panel) attained by a 1.0 $M_\oplus$ embryo embedded in a disk of N_{pln} equal-massed planetesimals for 1.0 Myr. N_{pln} is varied in each simulation, while the total mass of planetesimals is fixed at 1.0 $M_\oplus$.

at 1 au within a distribution of planetesimals with a total mass of 1 $M_\oplus$. We place the large planet on a moderately excited initial orbit ($e = 0.1$, $i = 5\overset{\circ}{.}0$), and in all cases, the orbit is markedly damped after 1 Myr. However, simulations using a smaller number of large planetesimals experience significantly greater damping and display a larger range of outcomes than those with a greater number of small planetesimals (although the total planetesimal mass remains fixed; see also Jacobson & Morbidelli 2014; Kobayashi et al. 2019).

We continue to test this concept with an additional suite of 50 simulations (see Table 4) of the classic terrestrial planet formation model (e.g., Chambers 2001, described in detail in Section 2.4). In 25 simulations, the planetesimal population is modeled using 1000 objects, each with mass $M = 0.0025\ M_\oplus$. Our second set of 25 simulations considers 2000 planetesimals with $M = 0.00125\ M_\oplus$. Each batch of simulations concludes with nearly identical mean AMD values (0.0101 and 0.0104, respectively, see Figure 11) that are about six times that of the modern solar system. However, the set of simulations employing fewer and large planetesimals has a greater dispersion of AMD outcomes ($\mathrm{min}_{1000} = 0.0014$, $\mathrm{max}_{1000} = 0.024$, $\sigma_{1000} = 0.0072$, $\mathrm{min}_{2000} = 0.0052$, $\mathrm{max}_{2000} = 0.018$, and $\sigma_{2000} = 0.0035$, see Figure 11). Thus, a terrestrial system forming within a distribution of larger planetesimals is able to randomly walk to both lower and higher AMD values. If we are to define "success" as satisfying a constraint 50% of the time (Nesvorný & Morbidelli 2012), most terrestrial formation models (with the notable exception of Grand Tack evolutionary schemes; Walsh et al. 2011; Walsh & Levison 2016) struggle to consistently replicate the solar system's low AMD. Because we find smaller populations of more massive planetesimals to be more successful at producing low AMD terrestrial planets, we argue that a primordial terrestrial disk of $r \sim 100$ km planetesimals (but not similar to the planetesimals used in our $N_{\mathrm{pln}} = 1000$ simulations) formed directly via gravitational instability (e.g., Morbidelli et al. 2009; Johansen et al. 2015) is worth investigating.

4. Conclusions

We present detailed simulations of embryo formation within a decaying gas disk starting from $r \sim 100$ km planetesimals. Our calculations begin by following oligarchic growth within individual radial annuli. As the total particle number decreases in each annulus, we interpolate within the intra-annulus regions, and assemble the entire terrestrial disk ($0.48 < a < 4.0$ au) in a single simulation after 1 Myr. Thus, our results are somewhat biased by our interpolation method (although we find this error term to be minor). Specifically, future work should employ a logarithmic means of interpolating between different annuli, rather than a linear one. There are several important takeaways from our work and that of other recent high-N studies of embryo formation (Carter et al. 2015; Walsh & Levison 2019; Wallace & Quinn 2019).

4.1. Bimodal Makeup Depends on Radial Location

We show that the ratio of total mass in embryos to the total mass in planetesimals (R) existing around the time of gas-disk dispersal varies strongly with semimajor axis. In the Earth/Venus-forming region we find R values as high as ∼4.0, as compared with more moderate ratios (∼2.0) in the proto-Mars region, and low concentrations of embryos ($R \simeq 0.20$) in the primordial asteroid belt. We argue that the different values of R in each disk region can lead to a substantial differences in system outcome during follow-on evolution. For instance, high R values in the inner disk have been shown to increase the probability of forming Venus/Mercury analogs (Lykawka & Ito 2019), while more moderate ratios in the Mars-forming region can potentially help limit Mars' final mass in an early Nice Model scenario (Clement et al. 2018).

4.2. Few Giant Impacts in the Giant Impact phase

Perhaps the most striking difference between our generated distributions of embryos and planetesimals (as well as those from similar studies; Carter et al. 2015; Walsh & Levison 2019) and those assumed in classic terrestrial formation models (Chambers 2001; Raymond et al. 2009) is the advanced evolutionary state attained in the $a \lesssim 1.0$ au region during the nebular gas phase. In our simulations, only a handful of reasonably large ($0.1 \lesssim M \lesssim 0.4\ M_\oplus$) embryos grows in the Earth- and Venus-forming regions of the disk. Therefore, the giant impact phase of evolution ensues as a delayed instability (e.g., Walsh & Levison 2019), with Earth and Venus experiencing only a few giant impacts en route to attaining their modern masses. Given the limited growth experienced by such embryos in an additional simplified suite of simulations of the giant impact phase, we speculate that a dynamical trigger (the Nice Model instability; Tsiganis et al. 2005; Nesvorný & Morbidelli 2012; Clement et al. 2018) is required to spawn the ultimate series of impacts in the inner solar system.

4.3. Large Primordial Planetesimals Generate More Extreme AMDs

Finally, we perform an additional suite of test simulations to demonstrate the effects of the fossilized primordial planetesimal SFD on final terrestrial AMD. Planetesimal-embryo encounters tend to damp the orbits of protoplanets via a random walk toward lower eccentricities, inclinations, and total system AMDs. We show that larger encounters generated from a distribution of fewer more massive planetesimals allow a system to randomly walk toward both higher and lower values of AMD. Thus, we speculate that a primordial generation of massive planetesimals ($r \sim 100$ km, formed via gravitational instability; Morbidelli et al. 2009; Johansen et al. 2015) might be advantageous in the ultimate giant impact phase of terrestrial assembly in terms of more consistently yielding systems with solar-system-like final AMDs.

Our GPU simulations required nearly two years to complete on NVIDIA GK110 (K20X) "Kepler" accelerators, and represent close to the highest contemporaneous resolution achievable with a direct *N*-body algorithm. We have shown that the primordial sizes of planetesimals are somewhat fossilized at the end of the gas-disk phase; therefore implying that the selection of a particular initial particle mass can lead to significant differences in final system outcomes. Thus, it is imperative that future authors continue to push the limits of particle resolution as advances in computing power make such endeavors feasible.

M.S.C. and N.A.K. thank the National Science Foundation for support under award AST-1615975. N.A.K. also acknowledges support under NSF CAREER award 1846388. This research is part of the Blue Waters sustained-petascale computing project, which is supported by the National Science Foundation (awards OCI-0725070 and ACI-1238993) and the state of Illinois. Blue Waters is a joint effort of the University of Illinois at Urbana-Champaign and its National Center for Supercomputing Applications (Bode et al. 2013; Kramer et al. 2015). Further computing for this project was performed at the OU Supercomputing Center for Education and Research (OSCER) at the University of Oklahoma (OU). This work used the Extreme Science and Engineering Discovery Environment (XSEDE), which is supported by National Science Foundation grant number ACI-1548562. Specifically, it used the Bridges system, which is supported by NSF award number ACI-1445606, at the Pittsburgh Supercomputing Center (PSC: Nystrom et al. 2015). Additional computation for the work described in this paper was supported by Carnegie Science's Scientific Computing Committee for High-Performance Computing (hpc.carnegiescience.edu).

References

Abod, C. P., Simon, J. B., Li, R., et al. 2019, ApJ, 883, 192
Adachi, I., Hayashi, C., & Nakazawa, K. 1976, PThPh, 56, 1756
Asphaug, E., & Reufer, A. 2014, NatGe, 7, 564
Birnstiel, T., Klahr, H., & Ercolano, B. 2012, A&A, 539, A148
Bode, B., Butler, M., Dunning, T., et al. 2013, in Contemporary High Performance Computing, ed. J. S. Vetter (London: Chapman and Hall), 339
Bonsor, A., Leinhardt, Z. M., Carter, P. J., et al. 2015, Icar, 247, 291
Bottke, W. F., Nesvorný, D., Grimm, R. E., Morbidelli, A., & O'Brien, D. P. 2006, Natur, 439, 821
Brasser, R., Werner, S., & Mojzsis, S. 2020, Icar, 338, 113514
Briceño, C., Vivas, A. K., Calvet, N., et al. 2001, Sci, 291, 93
Bromley, B. C., & Kenyon, S. J. 2017, AJ, 153, 216
Canup, R. M. 2012, Sci, 338, 1052
Carrera, D., Gorti, U., Johansen, A., & Davies, M. B. 2017, ApJ, 839, 16
Carter, P. J., Leinhardt, Z. M., Elliott, T., Walter, M. J., & Stewart, S. T. 2015, ApJ, 813, 72
Chambers, J. 2006, Icar, 180, 496
Chambers, J. E. 1999, MNRAS, 304, 793
Chambers, J. E. 2001, Icar, 152, 205
Chambers, J. E. 2013, Icar, 224, 43
Chambers, J. E. 2016, ApJ, 825, 63
Chambers, J. E., & Wetherill, G. W. 2001, M&PS, 36, 381
Clement, M. S., Kaib, N. A., & Chambers, J. E. 2019a, AJ, 157, 208
Clement, M. S., Kaib, N. A., Raymond, S. N., Chambers, J. E., & Walsh, K. J. 2019b, Icar, 321, 778
Clement, M. S., Kaib, N. A., Raymond, S. N., & Walsh, K. J. 2018, Icar, 311, 340
Clement, M. S., Raymond, S. N., & Kaib, N. A. 2019c, AJ, 157, 38
Dauphas, N., & Pourmand, A. 2011, Natur, 473, 489
Deienno, R., Gomes, R. S., Walsh, K. J., Morbidelli, A., & Nesvorný, D. 2016, Icar, 272, 114
Deienno, R., Izidoro, A., Morbidelli, A., et al. 2018, ApJ, 864, 50
Deienno, R., Morbidelli, A., Gomes, R. S., & Nesvorný, D. 2017, AJ, 153, 153
Deienno, R., Walsh, K. J., Kretke, K. A., & Levison, H. F. 2019, ApJ, 876, 103
Delbo, M., Avdellidou, C., & Morbidelli, A. 2019, A&A, 624, A69
Delbo', M., Walsh, K., Bolin, B., Avdellidou, C., & Morbidelli, A. 2017, Sci, 357, 1026
Dermott, S. F., Christou, A. A., Li, D., Kehoe, T. J. J., & Robinson, J. M. 2018, NatAs, 2, 549
Dominik, C., Blum, J., Cuzzi, J. N., & Wurm, G. 2007, in Protostars and Planets V, ed. B. Reipurth, D. Jewitt, & K. Keil (Tucson, AZ: Univ. Arizona Press), 783
Drążkowska, J., Alibert, Y., & Moore, B. 2016, A&A, 594, A105
Duncan, M. J., Levison, H. F., & Lee, M. H. 1998, AJ, 116, 2067
Fischer, R. A., & Ciesla, F. J. 2014, E&PSL, 392, 28
Gomes, R., Levison, H. F., Tsiganis, K., & Morbidelli, A. 2005, Natur, 435, 466
Grimm, S. L., & Stadel, J. G. 2014, ApJ, 796, 23
Haisch, K. E., Jr., Lada, E. A., & Lada, C. J. 2001, ApJL, 553, L153
Hansen, B. M. S. 2009, ApJ, 703, 1131
Hayashi, C. 1981, PThPS, 70, 35
Ida, S. 1990, Icar, 88, 129
Ida, S., & Guillot, T. 2016, A&A, 596, L3
Izidoro, A., Haghighipour, N., Winter, O. C., & Tsuchida, M. 2014, ApJ, 782, 31
Izidoro, A., Ogihara, M., Raymond, S. N., et al. 2017, MNRAS, 470, 1750
Izidoro, A., & Raymond, S. N. 2018, in Handbook of Exoplanets, ed. H. J. Deeg & J. A. Belmonte (New York: Springer), 2365, doi:10.1007/978-3-319-55333-7_142
Izidoro, A., Raymond, S. N., Morbidelli, A., & Winter, O. C. 2015, MNRAS, 453, 3619
Jackson, A. P., Gabriel, T. S. J., & Asphaug, E. I. 2018, MNRAS, 474, 2924
Jacobson, S. A., & Morbidelli, A. 2014, RSPTA, 372, 0174
Jacobson, S. A., Rubie, D. C., Hernlund, J., Morbidelli, A., & Nakajima, M. 2017, E&PSL, 474, 375
Johansen, A., & Lacerda, P. 2010, MNRAS, 404, 475
Johansen, A., mac Low, M.-M., Lacerda, P., & Bizzarro, M. 2015, SciA, 1, 1500109
Kaib, N. A., & Cowan, N. B. 2015, Icar, 252, 161
Kleine, T., Mezger, K., Palme, H., Scherer, E., & Münker, C. 2005, GeCoA, 69, 5805
Kleine, T., Touboul, M., Bourdon, B., et al. 2009, GeCoA, 73, 5150
Kobayashi, H., & Dauphas, N. 2013, Icar, 225, 122
Kobayashi, H., Isoya, K., & Sato, Y. 2019, ApJ, 887, 226
Kokubo, E., & Ida, S. 1995, Icar, 114, 247
Kokubo, E., & Ida, S. 1996, Icar, 123, 180
Kokubo, E., & Ida, S. 1998, Icar, 131, 171
Kokubo, E., & Ida, S. 2000, Icar, 143, 15
Kokubo, E., & Ida, S. 2002, ApJ, 581, 666
Kramer, W., Butler, M., Bauer, G., Chadalavada, K., & Mendes, C. 2015, in High Performance Parallel I/O, ed. Q. Prabhat & C. R. C. Koziol (Boca Raton, FL: CRC), 17
Kruijer, T. S., Kleine, T., Borg, L. E., et al. 2017, E&PSL, 474, 345
Lambrechts, M., & Johansen, A. 2014, A&A, 572, A107
Laskar, J. 1997, A&A, 317, L75
Lee, M. H., & Peale, S. J. 2002, ApJ, 567, 596
Leinhardt, Z. M., & Stewart, S. T. 2012, ApJ, 745, 79
Levison, H. F., Duncan, M. J., & Thommes, E. 2012, AJ, 144, 119

Levison, H. F., Kretke, K. A., Walsh, K. J., & Bottke, W. F. 2015, PNAS, 112, 14180
Levison, H. F., Morbidelli, A., Tsiganis, K., Nesvorný, D., & Gomes, R. 2011, AJ, 142, 152
Levison, H. F., Morbidelli, A., van Laerhoven, C., Gomes, R., & Tsiganis, K. 2008, Icar, 196, 258
Lissauer, J. J. 1987, Icar, 69, 249
Lykawka, P. S., & Ito, T. 2013, ApJ, 773, 65
Lykawka, P. S., & Ito, T. 2019, ApJ, 883, 130
Mastrobuono-Battisti, A., & Perets, H. B. 2017, MNRAS, 469, 3597
Milani, A., Knežević, Z., Spoto, F., et al. 2017, Icar, 288, 240
Mojzsis, S. J., Brasser, R., Kelly, N. M., Abramov, O., & Werner, S. C. 2019, ApJ, 881, 44
Morbidelli, A., Bottke, W. F., Nesvorný, D., & Levison, H. F. 2009, Icar, 204, 558
Morbidelli, A., Brasser, R., Gomes, R., Levison, H. F., & Tsiganis, K. 2010, AJ, 140, 1391
Morbidelli, A., Lambrechts, M., Jacobson, S., & Bitsch, B. 2015, Icar, 258, 418
Morbidelli, A., Lunine, J. I., O'Brien, D. P., Raymond, S. N., & Walsh, K. J. 2012, AREPS, 40, 251
Morbidelli, A., & Nesvorny, D. 2012, A&A, 546, A18
Morbidelli, A., Nesvorny, D., Laurenz, V., et al. 2018, Icar, 305, 262
Morishima, R., Stadel, J., & Moore, B. 2010, Icar, 207, 517
Nagasawa, M., Tanaka, H., & Ida, S. 2000, AJ, 119, 1480
Nesvorný, D. 2011, ApJL, 742, L22
Nesvorný, D. 2015a, AJ, 150, 73
Nesvorný, D. 2015b, AJ, 150, 68
Nesvorný, D., & Morbidelli, A. 2012, AJ, 144, 117
Nesvorný, D., & Vokrouhlický, D. 2016, ApJ, 825, 94
Nesvorný, D., Vokrouhlický, D., Bottke, W. F., & Levison, H. F. 2018, NatAs, 2, 878
Nystrom, N. A., Levine, M. J., Roskies, R. Z., & Scott, J. R. 2015, in Proc. 2015 XSEDE Conf., Scientific Advancements Enabled by Enhanced Cyberinfrastructure, ed. G. D. Peterson (New York: ACM), 30, doi:10.1145/2792745.2792775
O'Brien, D. P., Morbidelli, A., & Bottke, W. F. 2007, Icar, 191, 434
O'Brien, D. P., Morbidelli, A., & Levison, H. F. 2006, Icar, 184, 39
Petit, J.-M., Morbidelli, A., & Chambers, J. 2001, Icar, 153, 338
Quarles, B. L., & Lissauer, J. J. 2015, Icar, 248, 318
Raymond, S. N., & Izidoro, A. 2017, SciA, 3, e1701138
Raymond, S. N., Izidoro, A., & Morbidelli, A. 2018, arXiv:1812.01033
Raymond, S. N., O'Brien, D. P., Morbidelli, A., & Kaib, N. A. 2009, Icar, 203, 644
Raymond, S. N., Quinn, T., & Lunine, J. I. 2006, Icar, 183, 265
Raymond, S. N., Quinn, T., & Lunine, J. I. 2007, AsBio, 7, 66
Richardson, D. C., Quinn, T., Stadel, J., & Lake, G. 2000, Icar, 143, 45
Roig, F., & Nesvorný, D. 2015, AJ, 150, 186
Rubie, D. C., Jacobson, S. A., Morbidelli, A., et al. 2015, Icar, 248, 89
Sandine, C. M., & Jacobson, S. A. 2019, AAS/Division of Dynamical Astronomy Meeting, 51, 5
Sarid, G., Stewart, S. T., & Leinhardt, Z. M. 2014, LPSC, 45, 2723
Stadel, J. G. 2001, PhD thesis, Univ. Washington
Stewart, S. T., & Leinhardt, Z. M. 2012, ApJ, 751, 32
Tanaka, H., Takeuchi, T., & Ward, W. R. 2002, ApJ, 565, 1257
Tera, F., Papanastassiou, D. A., & Wasserburg, G. J. 1974, E&PSL, 22, 1
Tobin, J. J., Sheehan, P., Megeath, S. T., et al. 2020, ApJ, 890, 130
Tsiganis, K., Gomes, R., Morbidelli, A., & Levison, H. F. 2005, Natur, 435, 459
Volk, K., & Malhotra, R. 2019, AJ, 158, 64
Wallace, J., Tremaine, S., & Chambers, J. 2017, AJ, 154, 175
Wallace, S. C., & Quinn, T. R. 2019, MNRAS, 489, 2159
Walsh, K. J. 2009, Natur, 457, 1091
Walsh, K. J., & Levison, H. F. 2016, AJ, 152, 68
Walsh, K. J., & Levison, H. F. 2019, Icar, 329, 88
Walsh, K. J., Morbidelli, A., Raymond, S. N., O'Brien, D. P., & Mandell, A. M. 2011, Natur, 475, 206
Weidenschilling, S. J. 1977a, Ap&SS, 51, 153
Weidenschilling, S. J. 1977b, MNRAS, 180, 57
Wetherill, G. W. 1978, in IAU Coll. 52, Protostars and Planets, ed. T. Gehrels & M. S. Matthews (Tucson, AZ: Univ. Arizona Press), 565
Wetherill, G. W. 1980a, ARA&A, 18, 77
Wetherill, G. W. 1980b, ARA&A, 18, 77
Wetherill, G. W. 1991, Sci, 253, 535
Wetherill, G. W. 1996, Ap&SS, 241, 25
Wetherill, G. W., & Stewart, G. R. 1993, Icar, 106, 190
Whipple, F. L. 1972, in From Plasma to Planet, ed. A. Elvius (New York: Wiley), 211
Wisdom, J., & Holman, M. 1991, AJ, 102, 1528
Xiang, C., Matthews, L. S., Carballido, A., & Hyde, T. W. 2019, arXiv:1911.04589